Sputtered (Fe,Mn)3O4 Spinel Oxide Thin Films for Micro-Supercapacitor

Bukola Jolayemi, Gaetan Buvat, Thierry Brousse, Pascal Roussel, Christophe Lethien

Sputtered $(Fe,Mn)_3O_4$ spinel oxide thin films for micro-supercapacitor

Bukola Jolayemi[1,2], Gaetan Buvat[1,2], Thierry Brousse[2,3], Pascal Roussel[4*] and Christophe Lethien[1,2,5*]

[1] Institut d'Electronique, de Microélectronique et de Nanotechnologies, Université de Lille, CNRS, Université Polytechnique Hauts-de-France, UMR 8520 - IEMN, F-59000 Lille, France

[2] Réseau sur le Stockage Electrochimique de l'Energie (RS2E), CNRS FR 3459, 33 rue Saint Leu, 80039 Amiens Cedex, France

[3] Nantes Université, CNRS, Institut des Matériaux de Nantes Jean Rouxel, IMN, F-44000 Nantes, France

[4] Unité de Catalyse et de Chimie du Solide (UCCS), Université de Lille, CNRS, Centrale Lille, Université d'Artois, UMR 8181 – UCCS, F-59000 Lille, France

[5] Institut Universitaire de France (IUF), Paris (France)

*Correspondence to: christophe.lethien@univ-lille.fr & pascal.roussel@univ-lille.fr

Keywords: ($(Mn,Fe)_3O_4$, thin films, sputtering, target poisoning, micro-supercapacitors, pseudocapacitance

ABSTRACT

The scaling up of wireless operating microelectronics for upcoming Internet of Things (IoT) applications demands high-performance micro-supercapacitors (MSCs) with corresponding high-energy and power capabilities. Indeed, this necessitates the quest for MSC's electrode materials capable of delivering high energy density at high charge/discharge rates. Many multicationic oxides, such as spinel manganese-iron compounds, demonstrate good pseudocapacitive properties as positive electrodes in conventional supercapacitors. However, fulfilling the required fabrication techniques is a challenge for their applications in MSCs. Hence, this study, for the first time, demonstrates the successful deposition of spinel Mn-Fe thin films on a functional platinum-based current collector. The deposition is achieved in a reactive oxygen environment via reactive DC magnetron sputtering techniques and subsequently annealed *ex-situ* at 600 °C in a nitrogen environment. The electrochemical signature in neutral 1 M Na_2SO_4 aqueous electrolyte is comparable to those reported for spinel type Mn-Fe bulk counterparts. The areal capacitance at 10 $mV.s^{-1}$ is 15.5 $mF.cm^{-2}$ for 1 µm thick film, exhibiting excellent coulombic efficiency (close to 100%) and long-term cycle stability after 10,000 cycles. Thus, the synthesis of the multicationic pseudocapacitive oxides via compatible microelectronic deposition methods has set a prospective path to achieve very high-performance MSCs for future IoT applications.

INTRODUCTION

Powering the upcoming Internet of Things (IoT) technology based on miniaturized electronics devices in various domains require to improve the Technological Readiness Level (TRL) of on chip harvesting and storage microsystems to meet the performance demands and to ensure self-powered system with limited human intervention [1]. To fulfil the energy requirements, an attractive solution consists in combining harvested energy coming from the environment (for example: issued from solar, motion, thermal, or radiofrequency sources) with miniaturized electrochemical energy storage devices [2]. In the last few years, the development and integration of onboard electrochemical energy storage (EES) systems, notably metal-ion (Li-ion, Na-ion, etc.) micro-batteries (MBs) and micro-supercapacitors (MSCs) with a footprint surface close to a very few millimetres square have drawn lots of attention [3]–[5]. As such, MSCs are characterized by high power density (>10 $mW.cm^{-2}$) with high rate capability and long cycle life (> 100 000 cycles) but very low energy density (<0.1 $mWh.cm^{-2}$) while MBs offer high energy density (1 $mWh.cm^{-2}$) but low cycling lifetime (< 10 000 cycles) [1]. MSCs and MBs are complementary features needed for IoT devices. Nevertheless, the low technological maturity of MSCs hampers the scaling up of the pilot production line. Indeed, optimizing the energy density without compromising the power density (and cycle life), and the use of deposition techniques of active materials that are compatible with microfabrication techniques are among the most important key issues for the MSCs [1]–[3], [6]. Consequently, in order to scale up the fabrication process of micro-supercapacitors, the electrode materials, the electrolyte and the current collectors have to be deposited as thin films using deposition technique compatible with semiconductor processing facilities. This was achieved for binary metal nitride (vanadium nitride [3,8], chromium nitride [10]) or for $FeWO_4$ [2]) where

the electrode materials were deposited by magnetron sputtering technique. More specifically, we have firstly demonstrated the synthesis of $FeWO_4$ films by magnetron sputtering as an efficient negative pseudocapacitive electrode (-0.6 up to 0 V vs Ag/AgCl) for MSC operating in aqueous neutral electrolyte (5M $LiNO_3$). Nevertheless, the cell voltage of MSC based on this $FeWO_4$ material is limited to only 0.6 V in a symmetric configuration ($FeWO_4$ // $FeWO_4$). To increase the cell voltage, it is thus mandatory to work in a asymmetric configuration where the multicationic $(Mn,Fe)_3O_4$ oxide deposited by magnetron sputtering is proposed as an interesting positive electrode materials in aqueous neutral electrolyte.

The energy density of MSCs is directly related to the product of the square of the cell voltage and its capacitance; hence maximizing either the cell voltage or/and the capacitance value will result in an increased energy density. Among the existing electrode materials, the fast and reversible faradic redox reactions occurring at the surface or subsurface of the pseudocapacitive electrode materials provide considerably superior capacitance and energy density as compared to the carbon based electrodes [1], [7]**.** A plethora of pseudocapacitive electrode materials made from thin film deposition methods is widely investigated. Noble or transition metal oxides (RuO_2, MnO_2) or transition metal nitride (VN, W_2N, CrN) has drawn a lot of attention this last ten years [3], [7]–[12]. The charge storage mechanism in pseudocapacitive electrodes is restricted by the narrow potential window in aqueous electrolytes due to thermodynamic breakdown potential of water molecules (1.23 V), restricting the cell voltage of the MSCs to about 1 V [2], [6], [13]. Recent research activities have continued to focus on extending the narrow potential window in aqueous electrolytes, increasing the mass loading while maintaining the same footprint area, and developing deposition techniques compatible with microelectronic facilities [1]–[3].

Among the oxide-based electrodes, RuO_2 and MnO_2 are electrochemically active in their amorphous and/or hydrous form and are mainly synthesized by electrodeposition for MSC application where thin film deposition techniques is mandatory from the upscaling point of view. Unfortunately, making hydrous RuO_2 or MnO_2 films rules out a large number of appropriate deposition techniques of the semiconductor industry like physical vapor deposition methods [2] working under vacuum atmosphere. In contrast, high-density multicationic oxides (ternary transition metal oxides) with one transition metal ion and one electrochemically active or inactive metal ions, have been widely investigated as an alternative solution with a promise of being compatible with semiconductor deposition techniques [2] to be integrated in a technological process on pilot production line. The co-existence of two different cations in a single crystal structure could improve the electrical and electrochemical performance via both higher electrical conductivity than their constituting binary metal oxides, and multiple oxidation states [14], [15]. Recent research has shown that Mn-based spinel, particularly $MnFe_2O_4$, demonstrate a wide working potential range in aqueous medium and a pseudocapacitance mechanism close to that of MnO_2, suggesting favourable properties for both high-energy and power applications [16]–[20]. However, most studies conducted on such compounds as electrode materials for electrochemical capacitor have been focused on bulk materials issued from a slurry of active materials mixed with conductive agent and binder (i.e. thick films) which have limited scope in MSC applications due to the non-compatibility of such synthesis process with cleanroom facilities [13], [16], [17], [19]–[22].

Here, we propose to develop Mn-based spinel thin films via reactive magnetron sputtering deposition technique (fully compatible with cleanroom usually encountered in microelectronic industry), to study and to optimize the structure/properties

relationships. Hence, establishing desirable and stable sputtering deposition conditions, which is a crucial prerequisite to prepare reproducible, high quality Mn-electrode films as thin as possible for MSC application with high performance metrics, is the major focus of this study. The deposition parameters as well as the condition of the post annealing deposition process were carefully studied to provide spinel Mn-based films with good electrochemical performance.

METHODS

Film preparation

Prior to the thin film deposition, a [100] oriented silicon wafer was preliminarily coated with a stacked layer of Al_2O_3 (80 nm) / Cr (3 nm) / Pt (50 nm). The Al_2O_3 layer was deposited by Atomic Layer Deposition (ALD) in a PicoSun R200 reactor and acts as a diffusion barrier layer to prevent the platinum silicide (Pt-Si) formation occurring during the annealing process [2], [23]–[25]. The Cr and Pt layers were successively evaporated on the oxide layer by Plassys MEB 550 S equipment, acting as adhesive (between the oxide and Pt) and current collector layers respectively. The spinel Mn-films were subsequently deposited from an equimolar Mn/Fe (50/50) metallic single target (diameter 4 inch, 99.95%, Neyco) on the Pt current collector using magnetron sputtering cluster CT200 from Alliance Concept.

The films were sputtered under a mixed argon-oxygen atmosphere at room temperature while operating power and target to substrate distance were fixed at 100 W and 6 cm respectively, and kept constant throughout the experiment. The films preparation was carried out in three steps. The first part was to investigate the effect of the oxygen content on the film phase composition and sputter-yield by increasing the reactive oxygen gas flow from 0 sccm to 3.5 sccm, keeping constant the argon flow at 50 sccm, the deposition time at 30 minutes and the operating pressure at 3×10^{-2}

mbar. In a second step, to study the reversibility, the deposition was repeated by reversing the oxygen gas flow from 3.5 sccm to 0 sccm. The second segment of the optimization process was devoted to the evolution of the film thickness, at an operating pressure of 3 x 10^{-2} mbar under mixed oxygen/argon (2/50 sccm) atmosphere, as well as the concomitant changes in the electrochemical behavior. Finally, the last segment studied the variation of the film porosity at different operating pressures of 1 x 10^{-2} mbar, 3 x 10^{-2} mbar and 5 x 10^{-2} mbar sputtered under mixed oxygen/argon (2/50 sccm) atmosphere; for performance comparison, the deposition time was systematically adjusted to obtain 1 µm film thickness for each pressure. All the as-deposited amorphous Mn-Fe films were *ex situ* annealed at 600 °C for 2 hours in a tubular horizontal furnace (Ceradel, TH1200/TML100/500/13-2z) under a pure nitrogen atmosphere to crystallise to the expected phase, the temperature was ramped up from room temperature to the annealing temperature with a heating rate of 10 °C.min^{-1} and was left cooled down to room temperature.

Structural analyses

The film crystal structure was analyzed by a Rigaku Smartlab diffractometer (9 kW rotating anode) in Bragg-Brentano configuration equipped with a Hypix detector using a Cu $K\alpha_{1+2}$ radiation to record the diffractograms in 1D mode at 0.01°.$step^{-1}$. A 2° out-of-plane offset was applied between the sample and the detector to suppress the strong substrate signals coming from the high intensity of the (100) silicon reflection [2]. An *in situ* high temperature X-ray diffraction (HT-XRD) analysis was performed using an Anton-Paar DHS1100 furnace on the sample sputtered at 3 x 10^{-2} mbar under mixed oxygen/argon (2/50 sccm) atmosphere to study the phase evolution of the sample with the temperature, simulating the annealing process. The film was heated from 50 °C to 850 °C under various atmospheres (air, vacuum (**Figure S2**) and nitrogen

Figure 2a), the scan and heating rates were set at 10 °·min^{-1} (between 2θ = 15° and 50°), and 3 °C·min^{-1}, respectively. The cell parameters were refined using the JANA 2006 crystallographic program [2].

Microstructural analyses

The film's cross-section and surface morphology views, as well as thicknesses evolution, were characterized by a scanning electron microscope (SEM, Zeiss Ultra 55). The images were processed using ImageJ software by examining the volume fraction of the films to estimate the percentage of porosity [26]–[28].

Electrochemical analyses

The electrochemical measurements were performed using a Multi-channel VMP3 potentiostat (Bio-Logic), and conducted in flat cells using a conventional three-electrode setup. Mn-Fe thin film, silver-silver chloride electrode (Ag/AgCl) and a platinum wire were assembled in neutral aqueous 1M Na_2SO_4 electrolyte as positive electrode, reference electrode and counter electrode respectively.

RESULTS AND DISCUSSION

Phase evolution of the sputtered Mn-Fe film

The spinel Mn-Fe film was obtained in a two-step procedure, i.e. sputtering deposition of the amorphous films on the Pt current collector in a first step, followed by a post-deposition *ex-situ* annealing to crystalize to the expected spinel phase (see **Fig. 1a**.) The annealing conditions value (600°C, under pure N_2 atmosphere) will be discussed later on. The relationship between the reactive oxygen content and the deposition rate of the films (made at room temperature) was first explored while keeping fixed several other deposition parameters (operating power, pressure, deposition time, and Ar flow of 100 W, 3 x 10^{-2} mbar, 30 min, and 50 sccm respectively) to establish the suitable sputtering parameters used to deposit manganese-iron films under reactive atmosphere. **Figure 1b** shows the evolution of the deposition rate with the O_2 flow. There is no linear relationship between the film thickness (i.e. the deposition rate) and the oxygen flow rate. This behaviour is in fact commonly observed in many reactive sputtering processes, as reported in the literature [29]–[31]. In summary, it can be observed during the reactive sputtering process (under Ar / O_2 atmosphere) that:

- the deposition rate is significantly high at low O_2 flow rate (called “metal mode”),

- an abrupt decrease of the deposition rate starting from 1 sccm is encountered (called “transition region”),

- and further increase of the reactive gas flow results in a noticeably flat low deposition rate (from 1.5 sccm upward, called “compound mode”).

This can be explained by the fact that at low supply, the reactive O_2 molecules readily find sufficient sputtered metal atoms (species) to react with, but further increase in O_2 flow leads to a formation of a compound on the surface of the target as there are fewer

metal atoms available to react with [32]–[34]. The drastic decrease of the film thickness (i.e. the deposition rate) between 1 sccm and 1.5 sccm (**Fig. 1c**) indicates that the target surface has become oxidized and is no longer purely metallic; this transition from the “metal mode” to the “compound mode” is characterized as target poisoning effect [31], [32], [35] which has to be managed in case of the deposition of oxide films by magnetron sputtering methods. Consequently, at a low oxygen flow rate, the deposited film is mainly metallic with a high deposition rate (*i.e.* metal mode), while at a sufficient oxygen flow rate, fewer sputtered species are available for reaction with the supplied gas, resulting to a lower deposition rate at the compound sputtering mode (*i.e.* reactive mode). In addition, at low O2 flow rate, a film delamination problem was encountered after post-deposition annealing (**Fig. S1**). The high stress occurring at the interface between the platinum layer and the (Mn, Fe) oxide film is probably responsible for this delamination process. Indeed, in the metallic mode, iron and manganese metals react with the platinum layer during the annealing process, as observed by XRD (**Fig. 1d**).

The deposition sequence was repeated in the reverse order, i.e. while decreasing the reactive O_2 gas flow from 3.5 down to 0 sccm, in order to study the plasma behaviour of the mixed argon-oxygen gas and the deposition process stability. The sputtering process did not immediately move to the metal mode (as observed between 1.0 and 1.5 sccm during the increasing cycle). Not surprisingly, a shift of the abrupt transition at a lower flow rate between 1 and 0.5 sccm is observed, giving rise to a closed-loop (hysteresis region) between 0.5 and 1.5 sccm with a relatively wide separation width (**Fig. 1b**). Such loops with a hysteresis effect has already been observed and the separation width between the two abrupt transitions denotes the width of the hysteresis region [29], [30], [33], [34], [36]. In contrast to phase formation at 1 sccm during increasing cycle, the obtained film indicate spinel manganese-iron phase at the same

flow rate during the decreasing cycle, as confirmed by XRD (**Fig. 1d**). It is very challenging to maintain a stable process in the transition mode region (O_2 flow rate close to 1.0 sccm) between the metallic and the reactive modes. Thus, we have to use conditions with an oxygen flow rate enabling both a stable deposition process and a single spinel phase. The structural behaviour of the films with different oxygen contents varying from 1.5 to 3.5 sccm were studied in details by XRD (**Fig. 2a**). The reflections at 2θ=40°, 46° and 67.5° corresponds to the (111), (200) and (220) lattice plane of the platinum layer (current collector) respectively (JCPDS PDF 00-004-0802), while the peak at 2θ=36° is due to the K_β X-ray emission line of the (111) platinum plane, as a high flux configuration was chosen (i.e. without monochromator, but with only a Ni filter) [37]. The remaining peaks (2θ = 18°, 30°, 35°, 56° and 62°) are characteristic of a cubic spinel structure which crystallized into the space group $\mathrm{Fd}\bar{3}m$, identified by the JCPDS card 01-074-2403 or 01-075-0035. The former corresponds to the $MnFe_2O_4$ phase, and the second to the $FeMn_2O_4$ structure: the theoretical diffractograms of these two phases ($Mn_xFe_{3-x}O_4$; x = 1 or 2) are similar, meaning that the XRD characterization method cannot distinguish between $MnFe_2O_4$ and Mn_2FeO_4. We decided to formulate this film $(Mn,Fe)_3O_4$, in good agreement with XRF and EDX chemical analyses performed on “thick” films (not shown here) indicating a 50-50 metal cation distribution. Thus, the experiment has clearly demonstrated that it is impossible to obtain a single phase in the metallic mode of the deposition process (O2 flow lower than 1 sccm). Likewise, obtaining a reproducible single spinel-type in the transition mode region (O2 flow around 1 sccm) is not practicable, due to the unstable sputtering process in this zone. Therefore, the deposition of a single Mn-Fe phase from a single Mn:Fe (1:1) metallic target is only obtainable in the reactive mode as confirmed by the XRD analysis (**Fig. 2a**).

A sample deposited with 2.0 sccm of O_2 flow (510 nm-thick) was afterward selected to determine the suitable post-deposition annealing conditions by performing *in situ* high-temperature X-ray diffraction (HT-XRD) analyses under various atmospheres. The choice of 2.0 sccm flow rate was to avoid the unstable deposition process region, and to be close enough to the transition mode to easily recover a pure metallic target. Phase evolution of the film heated from 50 °C to 850 °C was monitored in air, under vacuum (**Fig. S2,** supporting information), and under inert nitrogen gas environment (**Fig. 2b**) to determine the best post-deposition annealing conditions required to obtain a single Mn-Fe spinel phase. The SEM cross sections of the selected sample (as deposited and after HT-XRD experiment) are presented in **Figure 2c**. The as-deposited sample is amorphous and exhibits porous columnar structure with highly homogenous morphologies, which is typically expected using such sputtering conditions at this deposition pressure (3 x 10^{-2} mbar) according to the Thornton's structure zone model (SZM) [38]. After the heat treatment at 850 °C, the columnar morphology was completely collapsed and changed to a dense compact film, with reduced thickness by about 60 nm (from 510 nm to 450 nm). The XRD thermodiffractograms were recorded at the scan and heating rates of 10 °.min^{-1} (between 2θ = 15° and 50°), and 3 °C.min^{-1} respectively. Depending on the atmosphere in the furnace, the conclusions are significantly differents. For film heat-treated under air, the reflection peaks identified at 2θ = 33°, 38° and 49° in the low temperature region (between 50 °C and 600 °C) are assigned to the maghemite type cubic structure space group $Ia\overline{3}$ of $(\gamma\text{-Mn,Fe})_2O_3$ with the JCPDS card 01-039-0238 or 01-065-7467, corresponding to $\gamma\text{-}Fe_2O_3$ or $\gamma\text{-}Mn_2O_3$ respectively. The maghemite $\gamma\text{-}Fe_2O_3$ phase ultimately occurs at low-temperature (thermal) oxidation and is unstable, it easily coverts to hematite ($\alpha\text{-}Fe_2O_3$) phase or bixbyite ($\beta\text{-}Fe_2O_3$) phase when

subjected to thermal alteration [39]–[43]. In addition, γ-Mn_2O_3 is reported to behave similarly as γ-Fe_2O_3, and spontaneously transforms to α-Mn_2O_3 or β- Fe_2O_3 under heat treatment [44], [45]. At 600 °C, additional reflection peaks at 2θ = 23° and 45° were observed while the previous peaks had intensity surge, the diffraction patterns were indexed in a bixbyite type cubic structure with space group $Ia\bar{3}$ of $(Mn,Fe)_2O_3$ (JCPDS PDF 01-076-0076) (**Fig. S2**). The evolved bixbyite phase from maghemite phase could be attributable to the thermally induced transformation or alloying process between Fe_2O_3 and Mn_2O_3 during the HT-XRD analysis [46]–[48]. All other detected peaks are assigned to the Pt current collector.

In contrast, it is clearly seen that the films remained amorphous from 50 °C to 600 °C under vacuum or nitrogen atmosphere, where only Pt reflection peaks are detected. At 600 °C under primary vacuum, additional reflection peaks at 2θ = 18°, 30°, 35° and 42.5° were observed along that of bixbyite type cubic structure with space group $Ia\bar{3}$ of $(Mn,Fe)_2O_3$ observed in air, the additional peaks were indexed in a spinel type cubic structure with space group $Fd\bar{3}m$ of $(Mn,Fe)_3O_4$ (JCPDS PDF 01-074-2403; 01-075-0035), indicating a multiphase oxide film. On the contrary, a single spinel phase was detected, along with that of assigned to Pt, in flowing nitrogen environment (**Fig. 2b**). In summary, the atmosphere-controlled high temperature X-ray diffraction analysis has clearly shown that, under air, it is impossible to obtain the expected spinel structure. Similarly, a single (Fe,Mn)3O4 spinel phase would be difficult to obtain under vacuum during post-deposition annealing process. Therefore, it is clear that to obtain the expected spinel manganese-iron compound as a pure phase, both nitrogen gas environment and temperature higher than 600 °C are mandatory during the post-deposition.

To determine the optimal post-deposition annealing temperature, two Mn-Fe films (~ 500 nm-thick, O_2 flow rate = 2.0 sccm) were annealed at two different temperatures (600 and 700 °C respectively). The columnar structure observed in the amorphous film is preserved even after the post-deposition heat treatment at both 600 °C and 700 °C (**Fig. 3a**), but a discernible modification of the porosity was observed with a slight distortion of the self-organized columns at 600 °C. However, when the annealing temperature was raised to 700 °C, a small shrinkage and larger columns (as compared to 600 °C) can be observed from the SEM micrograph, indicating a sintering process. The observed sintering process can be explained by coalescence phenomena where the inter-column spacing is reduced to form a larger column, resulting from the molecular movement through the continuous phase, due to the increased thermal energy [49]–[51]. The XRD main reflection peaks (2θ = 18°, 30°, 35°, 36.6°, 52°, 56° and 62°) are assigned to the $(Mn,Fe)_3O_4$ spinel structure (JCPDS card 01-074-2403 or 01-075-0035) while the remaining peaks are attributed to the platinum current collector(**Fig. 3b**). The electrochemical behaviour of the films was investigated by cyclic voltammetry (CV) in neutral aqueous electrolyte (1M Na_2SO_4) at different scan rates (**Fig. S4**). The CV curves of the films at 10 $mV.s^{-1}$ are displayed in **Figure 3c** and the corresponding extracted surface capacitance reported in **Figure 3d**. The quasi-rectangular CV curves measured between 0 and 1 V vs Ag/AgCl are comparable to those reported for bulk $(Mn,Fe)_3O_4$ in the literature [13].It was shown by *in situ* X-Ray Absorption studies, both at manganese and iron K-edges that the charge storage mechanism in crystalline $(Mn,Fe)_3O_4$ material involves charge transfer at both the Mn and Fe cations, balanced by the contribution of the proton coming from the KCl or NaCl aqueous electrolyte. Our study was performed in Na_2SO_4 aqueous neutral electrolyte; in that case, alkaline (Na+) ions and/or protons (H^+) could participate to the redox

process in our thin films. The large redox peaks observed in **Fig. 3c** within the 0.6 – 0.8 V potential ranges could be attributed to the charge transfer occurring at the Fe cation sites, as proposed by N. Wu *et al* [17], [52]. The surface capacitance values of the samples annealed at 600 °C and 700 °C respectively was evaluated at different scan rates from 2 up to 200 $mV.s^{-1}$. We observe that the areal capacitance (~15 $mF.cm^{-2}$ at 2 $mV.s^{-1}$) at 600 °C doubles that of the one measured (~7.5 $mF.cm^{-2}$ at 2 $mV.s^{-1}$) for the sample annealed at 700 °C, while the amount of active material (i.e. the film thickness) is similar (~ 500 nm) in the two cases. The sintering process occurring at 700 °C reduces the specific surface of the $(Mn,Fe)_3O_4$ films and thus the number of active sites easily accessible by the aqueous electrolyte. Considering the surface capacitance values of the 500 nm-thick $(Mn,Fe)_3O_4$ films annealed at 600 °C, the corresponding volumetric and gravimetric capacitance values are evaluated close to 300 $F.cm^{-3}$ and 75 $F.g^{-1}$ respectively taking into account a bulk density of 4 $g.cm^{-3}$ (corresponding to 80 % of the theoretical value (~5 $g.cm^{-3}$) owing to the porous morphology of the magnetron sputtered films). The gravimetric capacitance value is similar to the one measured by N. Wu *et al* on bulk $MnFe_2O_4$ powder electrode [17], [20], [52]. It can be noted that a capacitance of 15 $mF.cm^{-2}$ over a 1V potential window corresponds to 0.18 electron per mole of $(Mn,Fe)_3O_4$ films. Similar values (0.25 electron per mole of $MnFe_2O_4$ [17] and 0.17 electron per mol of MnO_2 [53]) were reported for powder-based electrodes. This clearly points out that not all the electrode material is affected by the electrochemical charge storage and that only a layer at the surface of the porous $(Mn,Fe)_3O_4$ films is electrochemically active.

Consequently, the optimized electrochemical performance of the $(Mn,Fe)_3O_4$ thin films were achieved using a 600 °C annealing temperature. The cycling stability of the sputtered films was evaluated in 1M Na_2SO_4 electrolyte and the capacity retention was

measured close to 100% after 10,000 cycles. A similar trend was observe for the coulombic efficiency (~ 100%) as depicted in **Fig. 3e** and the CV curves at 10^{th}, $1\,000^{th}$ and $10\,000^{th}$ cycles are shown in the inset of **Fig. 3e** showing the remarkable cycling performance of our sputtered $(Mn,Fe)_3O_4$ films.

Enhancement of the electrochemical performance with the thickness

After selecting the best oxygen flow rate and the post-deposition annealing conditions, the influence of the film thickness is put into perspective as a key parameter to maximize the electrode performance. The structural and microstructural properties of $(Mn,Fe)_3O_4$ films with different thicknesses (from 0.5 up to 4 µm) were characterized by XRD and cross section SEM analyses. The films were deposited at 3×10^{-2} mbar under mixed oxygen / argon (2 / 50 sccm) atmosphere at different deposition times followed by an *ex situ* annealing process under pure nitrogen environment at 600 °C for 2 hr. The linear dependence of the film thickness on the deposition time is illustrated in **Figure S3a** showing SEM cross sections of the amorphous films (**Fig. S3b**) with homogenous porous columnar morphologies. This microstructure is preserved after post-deposition heat treatment in all the samples (**Fig. 4a**). Concerning the XRD structural analysis, main peaks are assigned to both the $(Mn,Fe)_3O_4$ spinel structure (JCPDS card 01-074-2403 or 01-075-0035) and to the platinum current collector (**Fig. 3b**). The electrochemical behaviour of this series of annealed Mn-Fe spinel compound was also investigated by cyclic voltammetry (CV) in neutral aqueous electrolyte (1M Na_2SO_4) *vs* the film thickness at different scan rates (**Fig. S5**). The CV plots at 10 $mV.s^{-1}$ and the extracted surface capacitance values at different scan rates and thicknesses are displayed in **Figure 3c-e**. The representative CV shows the typical electrochemical signature of $MnFe_2O_4$ whatever the film thickness, taking into account a potential window ranging from 0 V to 1 V (v Ag/AgCl). The areal capacitance of the

films at 2 $mV.s^{-1}$ is ~15, ~25, ~40 and ~80 $mF.cm^{-2}$ for 500, 1120, 1900 and 3870 nm respectively. As expected, the surface capacitance value increases linearly with the thickness of the film [9] indicating thus that an increase of the mass loading improves the surface capacitance, which is in good agreement with the results reported by Robert et al. [8] for thin films electrodes made from sputtering deposition method. The surface capacitance values of the $(Mn,Fe)_3O_4$ electrode is compared vs state of the art values of binary and ternary oxide electrodes as well as nitride electrodes. RuO_2 films (~ 200 nm-thick) deposited with magnetron sputtering in 2001 [54] showed a surface capacitance value of ~ 15 $mF.cm^{-2}$ (taking into account a parallel plate configuration of a MSC with C_{MSC} ~ 7.5 $mF.cm^{-2}$). Manganese dioxide film was deposited by (Glancing angle deposition) GLAD technique (under vacuum) followed by an electrochemical oxidation process in 2002 [55] and ~ 400 nm-thick MnO_2 film showed a surface capacitance value close to ~ 50 $mF.cm^{-2}$ in 0.1M Na_2SO_4 electrolyte. T.M. Dinh has shown in 2015 [56] the electrodedeposition of MnO_2 films (~ 600 nm-thick) on gold current collector and the surface capacitance value does not exceed 24.5 $mF.cm^{-2}$ (~ 22 $mC.cm^{-2}$ over 0.9 V). The $FeWO_4$ electrodes made by magnetron sputtering method in 2021 [3] by our group shows a surface capacitance value close to ~ 5 $mF.cm^{-2}$. Consequently, the obtained surface capacitances of $(Mn, Fe)_3O_4$ films (~ 80 $mF.cm^{-2}$) are among the best reported values up to now in the field of oxide-based electrodes grown by thin film deposition technique. Nevertheless, the density (and thus the porosity respectively) of such electrode stays at a high level (low level) for metal oxides deposited by magnetron sputtering technique (at room temperature) owing to the post annealing process used to crystallize the as-deposited amorphous film in the expected electroactive phase thus leading to a densification process. This is not the case of transition metal nitride electrodes made from sputtering technique [2, 8-10, 12] where

the as-deposited films are already crystallized when deposited at room temperature. Moreover, these nitrides films exhibit a high level of intra & intercolumnar porosities within the film microstructure [3, 8, 12]. In that case, the surface capacitance values of nitride-based electrodes could reached more than 1 $F.cm^{-2}$ when pseudocapacitive material is considered.

To improve the cell voltage and thus the energy density of a MSC, an attractive solution consists in coupling the proposed $(Mn, Fe)_3O_4$ electrode (positive potential, from 0 up to 1 V vs Ag/AgCl) together with a $FeWO_4$ electrode (negative potential, from -0.6 up to 0 V vs Ag/AgCl) in neutral aqueous electrolyte. In that case – and taking into account a good charge balancing between the two electrodes - it will be expected to reach at least 1.6 V cell voltage. This asymmetric coupling constitutes a mid-term action as a perspective of this work.

Tuning the film porosity with the sputtering deposition pressure

An attractive solution to control the performance of thin films electrode made from capacitive materials consists in tuning the film porosity (or the density). To reach this goal, our group has already demonstrated that deposition pressure is a key parameter either for Li-ion micro-batteries or micro-supercapacitors applications [3], [8], [57]–[61]. Sputtering under high pressure has shown to favour growth films with columnar microstructure [3], [62], [63]. The feasibility to synthesize the spinel phase has been demonstrated in the previous part; this part will be devoted to study the influence of the deposition pressure on the porous microstructure of the films and their corresponding electrochemical performance. The targeted film thickness is about 1 µm. For a sake of clarity, to obtain three samples showing the same thickness but deposited at various pressures, the deposition time was modified (3 hours, 3.5 hours and 5 hours regarding a pressure of 1 x 10^{-2} mbar, 3 x 10^{-2} mbar and 5 x 10^{-2} mbar

respectively (**Figure S6**)). The other deposition parameters were kept constant (power = 100 W, oxygen / argon ratio = 2 / 50 sccm respectively, deposition at room temperature, *ex situ* annealed at 600 °C for 2 hours under a pure N_2 environment). The film thickness was about 1 µm for all the deposited films as depicted in **Figure 5a**. Porous columnar structure with homogenous morphologies was observed with varying degree of porosity: the percentage of porosity was estimated from the SEM top view images using an image analysis software (ImageJ). This percentage was estimated to 5, 17 and 25 % for the samples deposited at 10^{-2} mbar, 3 x 10^{-2} mbar and 5 x 10^{-2} mbar, respectively (**Fig. 5b**). At 10^{-2} mbar, as expected, columnar microstructure of the $(Mn,Fe)_3O_4$ film is found to be less porous, and become more porous for higher pressures. This result strongly agrees with literature that reports that deposited films are denser at low deposition pressure due to the atomic peening effect resulting from high energy atoms bombardment on the film surface, thereby inducing atomic re-sputtering in the column boundaries [8], [37]. As such, the columns become larger with the increasing pressure after post-deposition heat treatment, leading to increased specific surface area (**Fig. 5b**, inset). All the samples crystallize to the $(Mn,Fe)_3O_4$ spinel structure (JCPDS card 01-074-2403 or 01-075-0035) (**Fig. 5c**). The lattice parameters (obtained by LeBail refinement) were refined from the XRD analyses and are to 8.4974(7) Å, 8.5154(5) Å and 8.5185(12) Å for the samples deposited at 10^{-2}, 3 x 10^{-2} and 5 x 10^{-2} mbar respectively. These values, close to the theoretical one (8.511 Å), slightly increase with the deposition pressure, are consistent with previous studies reported in the literature [64]–[66]. The electrochemical behaviour of the different films exhibits quasi-rectangular CV curves at the various pressures, typically observed for a capacitive material (**Fig. 5d**). The surface capacitance evaluated at 10 $mV.s^{-1}$ are close to ~ 11 $mF.cm^{-2}$, ~ 15.5 $mF.cm^{-2}$, and ~14.5 $mF.cm^{-2}$ for the samples deposited at 10^{-}

^{2} mbar, 3 x 10^{-2} mbar and 5 x 10^{-2} mbar respectively (**Fig. 5e and fig. S7**). The areal capacitance increases when the pressure increases up to 3 x 10^{-2} mbar but stabilizes when the pressure is set to 5 x 10^{-2} mbar whatever the sweep rates as shown in **Figure 5d-e**.

CONCLUSION

Synthesis of spinel manganese-iron$(Mn,Fe)_3O_4$ thin films has been successfully achieved by a two-step procedure: an amorphous film is first deposited by reactive magnetron sputtering deposition method on Si / Al_2O_3 / Cr-Pt current collector followed by a post-deposition *ex-situ* annealing step under nitrogen atmosphere, needed to crystallize in the expected spinel phase. The electrochemical behaviour tested in neutral aqueous electrolyte demonstrates characteristic pseudocapacitive CV curves comparable to those reported for $MnFe_2O_4$ bulk counterparts. The long-term cycle stability indicates that $(Mn,Fe)_3O_4$ thin film electrodes are promising for MSCs applications, though the obtained surface capacitance values are still low compared to values obtained for transition metal nitride electrodes. This work is also confirming our recent findings on sputtered $FeWO_4$, i.e. that multicationic oxide thin films can be implemented as electrodes for micro-supercapacitor application, using deposition methods compatible with microelectronic facilities. Further studies on this multicationic oxide compounds will be focused on the evaluation of the electroactive cation(s) within the $(Mn,Fe)_3O_4$ films.

ACKNOWLEDGMENTS

The authors want to thank the French network on electrochemical energy storage (RS2E) and the Store-Ex Labex for the support. The French RENATECH network and the University of Lille are greatly acknowledged for the supporting the Center of

MicroNanoFabrication (CMNF) facility. Chevreul Institute (FR 2638), Ministère de l'Enseignement Supérieur et de la Recherche, Région Hauts de France and FEDER are acknowledged for supporting and funding XRD facility.

DATA AVALAIBILITY

COMPETING INTERESTS

The authors declare no competing interests.

MATERIALS & CORRESPONDENCE

Correspondence to Christophe Lethien & Pascal Roussel

REFERENCES

[1] C. Lethien, J. le Bideau, and T. Brousse, “Challenges and prospects of 3D micro-supercapacitors for powering the internet of things,” *Energy and Environmental Science*, vol. 12, no. 1. Royal Society of Chemistry, pp. 96–115, Jan. 01, 2019. doi: 10.1039/c8ee02029a.

[2] G. Buvat, A. Iadecola, F. Blanchard, T. Brousse, P. Roussel, and C. Lethien, “ A First Outlook of Sputtered FeWO4 Thin Films for Micro-Supercapacitor Electrodes ,” *Journal of The Electrochemical Society*, vol. 168, no. 3, p. 030524, Mar. 2021, doi: 10.1149/1945-7111/abec57.

[3] K. Robert, D. Stiévenard, D. Deresmes, C. Douard, A. Iadecola, D. Troadec, P. Simon, N. Nuns, M. Marinova, M. Huvé, P. Roussel, T. Brousse and C. Lethien, “Novel insights into the charge storage mechanism in pseudocapacitive vanadium nitride thick films for high-performance on-chip micro-supercapacitors,” *Energy and Environmental Science*, vol. 13, no. 3, pp. 949–957, Mar. 2020, doi: 10.1039/c9ee03787j.

[4] L. Liu, Q. Weng, X. Lu, X. Sun, L. Zhang, OG. Schmidt, “Advances on Microsized On-Chip Lithium-Ion Batteries,” *Small*, vol. 13, no. 45, p. 1701847, Dec. 2017, doi: 10.1002/SMLL.201701847.

[5] A. Ferris, D. Bourrier, S. Garbarino, D. Guay, D. Pech, “3D Interdigitated Microsupercapacitors with Record Areal Cell Capacitance,” *Small*, vol. 15, no. 27, p. 1901224, Jul. 2019, doi: 10.1002/SMLL.201901224.

[6] Y. Shao, M.F El-Kady, J. Sun, Y. Li, Q. Zhang, M. Zhu, H. Wang, B. Dunn and R. B. Kaner., “Design and Mechanisms of Asymmetric Supercapacitors,” *Chemical Reviews*, vol. 118, no. 18. American Chemical Society, pp. 9233–9280, Sep. 26, 2018. doi: 10.1021/acs.chemrev.8b00252.

[7] Y. Zhang, L. Li, H. Su, W. Huang, and X. Dong, “Binary metal oxide: Advanced energy storage materials in supercapacitors,” *Journal of Materials Chemistry A*, vol. 3, no. 1. Royal Society of Chemistry, pp. 43–59, Jan. 07, 2015. doi: 10.1039/c4ta04996a.

[8] K. Robert, C. Douard, A. Demortière, F. Blanchard, P. Roussel, T. Brousse and C. Lethien., “On Chip Interdigitated Micro-Supercapacitors Based on Sputtered Bifunctional Vanadium Nitride Thin Films with Finely Tuned Inter- and Intracolumnar Porosities,” *Advanced Materials Technologies*, vol. 3, no. 7, Jul. 2018, doi: 10.1002/ADMT.201800036.

[9] B. Asbani, K. Robert, P. Roussel, T. Brousse, and C. Lethien, “Asymmetric micro-supercapacitors based on electrodeposited Ruo2 and sputtered VN films,” *Energy Storage Materials*, vol. 37, pp. 207–214, May 2021, doi: 10.1016/J.ENSM.2021.02.006.

[10] E. Haye , A. Achour, A. Guerra, F. Moulaïb, T. Hadjersi, R. Boukherroub, A. Panepinto, T. Brousse, J.J. Pireaux, S. Lucas, “Achieving on chip micro-supercapacitors based

on CrN deposited by bipolar magnetron sputtering at glancing angle," *Electrochimica Acta*, vol. 324, p. 134890, Nov. 2019, doi: 10.1016/J.ELECTACTA.2019.134890.

[11] H. Liu, W. He, X. Wang, Z. Lan, and H. Xu, "Sputtered chromium nitride/carbon nanotubes hybrid structure for electrochemical capacitors," *Applied Physics A: Materials Science and Processing*, vol. 127, no. 2, pp. 1–8, Feb. 2021, doi: 10.1007/S00339-020-04264-0/FIGURES/9.

[12] C. Choi, K. Robert, G. Whang, P. Roussel, C. Lethien, and B. Dunn, "Photopatternable hydroxide ion electrolyte for solid-state micro-supercapacitors," *Joule*, vol. 5, no. 9, pp. 2466–2478, Sep. 2021, doi: 10.1016/J.JOULE.2021.07.003.

[13] R. Wang, Q. Li, L. Cheng, H. Li, B. Wang, X.S. Zhao, P. Guo, "Electrochemical properties of manganese ferrite-based supercapacitors in aqueous electrolyte: The effect of ionic radius," *Colloids and Surfaces A: Physicochemical and Engineering Aspects*, vol. 457, no. 1, pp. 94–99, Sep. 2014, doi: 10.1016/j.colsurfa.2014.05.059.

[14] M.C Liu, L.B Kong, L. Kang, X. Li, F.C. Walsh, M. Xing, C. Lu, X.J Ma and Y.C Luo, "Synthesis and characterization of M3V2O8 (M = Ni or Co) based nanostructures: A new family of high performance pseudocapacitive materials," *Journal of Materials Chemistry A*, vol. 2, no. 14, pp. 4919–4926, Apr. 2014, doi: 10.1039/c4ta00582a.

[15] C. An, Y. Zhang, H. Guo, and Y. Wang, "Metal oxide-based supercapacitors: progress and prospectives," *Nanoscale Advances*, vol. 1, no. 12. Royal Society of Chemistry, pp. 4644–4658, 2019. doi: 10.1039/c9na00543a.

[16] C. Wei, Z. Feng, M. Baisariyev, L. Yu, L. Zeng, T. Wu H. Zhao, Y. Huang, M.J. Bedzyk, T. Sritharan and Z. J. Xu, "Valence Change Ability and Geometrical Occupation of Substitution Cations Determine the Pseudocapacitance of Spinel Ferrite XFe2O4(X = Mn, Co, Ni, Fe)," *Chemistry of Materials*, vol. 28, no. 12, pp. 4129–4133, Jun. 2016, doi: 10.1021/acs.chemmater.6b00713.

[17] S.-L. Kuo, J.-F. Lee, and N.-L. Wu, "Study on Pseudocapacitance Mechanism of Aqueous MnFe2O4 Supercapacitor," *Journal of The Electrochemical Society*, vol. 154, no. 1, p. A34, 2007, doi: 10.1149/1.2388743.

[18] M. L. Aparna, A. N. Grace, P. Sathyanarayanan, and N. K. Sahu, "A comparative study on the supercapacitive behaviour of solvothermally prepared metal ferrite (MFe2O4, M = Fe, Co, Ni, Mn, Cu, Zn) nanoassemblies," *Journal of Alloys and Compounds*, vol. 745, pp. 385–395, May 2018, doi: 10.1016/j.jallcom.2018.02.127.

[19] V. Vignesh, K. Subramani, M. Sathish, and R. Navamathavan, "Electrochemical investigation of manganese ferrites prepared via a facile synthesis route for supercapacitor applications," *Colloids and Surfaces A: Physicochemical and Engineering Aspects*, vol. 538, pp. 668–677, Feb. 2018, doi: 10.1016/j.colsurfa.2017.11.045.

[20] S. L. Kuo and N. L. Wu, "Electrochemical capacitor of MnFe2O4 with NaCl electrolyte," *Electrochemical and Solid-State Letters*, vol. 8, no. 10, 2005, doi: 10.1149/1.2008847.

[21] S. L. Kuo and N. L. Wu, “Electrochemical characterization on MnFe2O4/carbon black composite aqueous supercapacitors,” *Journal of Power Sources*, vol. 162, no. 2, pp. 1437–1443, Nov. 2006, doi: 10.1016/J.JPOWSOUR.2006.07.056.

[22] S. Nagamuthu, S. Vijayakumar, S. H. Lee, and K. S. Ryu, “Hybrid supercapacitor devices based on MnCo2O4 as the positive electrode and FeMn2O4 as the negative electrode,” *Applied Surface Science*, vol. 390, pp. 202–208, Dec. 2016, doi: 10.1016/J.APSUSC.2016.08.072.

[23] J. C. Taylor, “Platinum metallization on silicon and silicates,” *Journal of Materials Research*, vol. 36, no. 1. Springer Nature, pp. 211–234, Jan. 01, 2021. doi: 10.1557/s43578-020-00084-3.

[24] M. Hallot, A. Demortière, P. Roussel, and C. Lethien, “Sputtered LiMn1.5Ni0.5O4 thin films for Li-ion micro-batteries with high energy and rate capabilities,” *Energy Storage Materials*, vol. 15, pp. 396–406, Nov. 2018, doi: 10.1016/j.ensm.2018.08.012.

[25] M. Létiche, M. Hallot, M. Huvé, T. Brousse, P. Roussel, and C. Lethien, “Tuning the Cation Ordering with the Deposition Pressure in Sputtered LiMn1.5Ni0.5O4 Thin Film Deposited on Functional Current Collectors for Li-Ion Microbattery Applications,” *Chemistry of Materials*, vol. 29, no. 14, pp. 6044–6057, Jul. 2017, doi: 10.1021/acs.chemmater.7b01921.

[26] B. Yao and K. R. Coffey, “Quantification of L10 phase volume fraction in annealed [Fe/Pt]n multilayer films,” *Journal of Applied Physics*, vol. 105, no. 3, 2009, doi: 10.1063/1.3068364.

[27] H. Zhang, C. Li, , M. Xu, W.Dai, P. Kumar, Z. Liu, Z. Li, Y. Zhang., “The fatigue performance evaluation of additively manufactured 304L austenitic stainless steels,” *Materials Science and Engineering A*, vol. 802, Jan. 2021, doi: 10.1016/j.msea.2020.140640.

[28] Y. Wu, P. Tahmasebi, C. Lin, M. Aleem Zahid, C. Dong, A. N. Golab, L. Ren, “A comprehensive study on geometric, topological and fractal characterizations of pore systems in low-permeability reservoirs based on SEM, MICP, NMR, and X-ray CT experiments,” *Marine and Petroleum Geology*, vol. 103, pp. 12–28, May 2019, doi: 10.1016/j.marpetgeo.2019.02.003.

[29] S. Berg and T. Nyberg, “Fundamental understanding and modeling of reactive sputtering processes,” *Thin Solid Films*, vol. 476, no. 2. Elsevier, pp. 215–230, Apr. 08, 2005. doi: 10.1016/j.tsf.2004.10.051.

[30] W. D. Sproul, D. J. Christie, and D. C. Carter, “Control of reactive sputtering processes,” *Thin Solid Films*, vol. 491, no. 1–2. pp. 1–17, Nov. 22, 2005. doi: 10.1016/j.tsf.2005.05.022.

[31] J. Musil, P. Baroch, J. Vlček, K. H. Nam, and J. G. Han, “Reactive magnetron sputtering of thin films: Present status and trends,” in *Thin Solid Films*, Mar. 2005, vol. 475, no. 1-2 SPEC. ISS., pp. 208–218. doi: 10.1016/j.tsf.2004.07.041.

[32] A. H. Simon, “Sputter Processing,” in *Handbook of Thin Film Deposition: Techniques, Processes, and Technologies: Third Edition*, Elsevier Inc., 2012, pp. 55–88. doi: 10.1016/B978-1-4377-7873-1.00004-8.

[33] M. Arif and C. Eisenmenger-Sittner, “In situ assessment of target poisoning evolution in magnetron sputtering,” *Surface and Coatings Technology*, vol. 324, pp. 345–352, Sep. 2017, doi: 10.1016/j.surfcoat.2017.05.047.

[34] M. Fekete, K. Bernátová, P. Klein, J. Hnilica, and P. Vašina, “Influence of sputtered species ionisation on the hysteresis behaviour of reactive HiPIMS with oxygen admixture,” *Plasma Sources Science and Technology*, vol. 29, no. 2, Feb. 2020, doi: 10.1088/1361-6595/ab5f2b.

[35] P. Mareš, S. Kadlec, M. Dubau, A. Marek, and J. Vyskočil, “Long-term stability and disappearing anode effects during reactive DC and pulsed bipolar magnetron sputtering of Al2O3,” *Vacuum*, vol. 173, Mar. 2020, doi: 10.1016/j.vacuum.2019.109161.

[36] D. Güttler, B. Abendroth, R. Grötzschel, W. Möller, and D. Depla, “Mechanisms of Target Poisoning during Magnetron Sputtering as Investigated by Real-Time in situ Analysis and Collisional Computer Simulation.”

[37] M. Létiche, M. Hallot, M. Huvé, T. Brousse, P. Roussel, and C. Lethien, “Tuning the Cation Ordering with the Deposition Pressure in Sputtered LiMn1.5Ni0.5O4 Thin Film Deposited on Functional Current Collectors for Li-Ion Microbattery Applications,” *Chemistry of Materials*, vol. 29, no. 14, pp. 6044–6057, Jul. 2017, doi: 10.1021/acs.chemmater.7b01921.

[38] J. A. Thornton, “The microstructure of sputter-deposited coatings,” *Journal of Vacuum Science & Technology A: Vacuum, Surfaces, and Films*, vol. 4, no. 6, pp. 3059–3065, Nov. 1986, doi: 10.1116/1.573628.

[39] J. Lee and S. Y. Kwak, “Mn-Doped Maghemite (γ-Fe2O3) from Metal-Organic Framework Accompanying Redox Reaction in a Bimetallic System: The Structural Phase Transitions and Catalytic Activity toward NOx Removal,” *ACS Omega*, vol. 3, no. 3, pp. 2634–2640, Mar. 2018, doi: 10.1021/ACSOMEGA.7B01865/ASSET/IMAGES/LARGE/AO-2017-01865A_0005.JPEG.

[40] X. Liu, H. Li, Y. Fang, and Z. Yang, “Heterogeneous catalytic ozonation of sulfamethazine in aqueous solution using maghemite-supported manganese oxides,” *Separation and Purification Technology*, vol. 274, p. 118945, Nov. 2021, doi: 10.1016/J.SEPPUR.2021.118945.

[41] J. Lai, K. V. P. M. Shafi, K. Loos, A. Ulman, Y. Lee, T. Vogt, and C. Estournès., “Doping γ-Fe2O3 nanoparticles with Mn(III) suppresses the transition to the α-Fe2O3 structure,” *J Am Chem Soc*, vol. 125, no. 38, pp. 11470–11471, Sep. 2003, doi: 10.1021/JA035409D/SUPPL_FILE/JA035409DSI20030623_040336.PDF.

[42] M. W. McElhinny and P. L. McFadden, “Paleomagnetism: Continents and Oceans (Chapter Two - Rock Magnetism),” *International Geophysics*, vol. 73, no. C, pp. 31–77, Jan. 2000, doi: 10.1016/S0074-6142(00)80095-9.

[43] B. M. Moskowitz, M. Jackson, and V. Chandler, “Geophysical Properties of the Near-Surface Earth: Magnetic Properties,” *Treatise on Geophysics: Second Edition*, vol. 11, pp. 139–174, Jan. 2015, doi: 10.1016/B978-0-444-53802-4.00191-3.

[44] Z. Bai, Y. Zhang, Y. Zhang, C. Guo, B. Tang, and D. Sun, “MOFs-derived porous Mn2O3 as high-performance anode material for Li-ion battery,” *Journal of Materials Chemistry A*, vol. 3, no. 10, pp. 5266–5269, Feb. 2015, doi: 10.1039/C4TA06292B.

[45] R. D. W. Kemmitt and R. D. Peacock, *The chemistry of manganese*, 1st ed., vol. 13. Oxford: Pergomon Press, 1973.

[46] D. Ghosh, U. Dutta, A. Haque, N. E. Mordvinova, O. I.Lebedev, K. Pal, A. Gayen, P. Mahata, A. K. Kundu, Md. M. Seikh, “Evidence of low temperature spin glass transition in bixbyite type FeMnO3,” *Materials Science and Engineering: B*, vol. 226, pp. 206–210, Dec. 2017, doi: 10.1016/J.MSEB.2017.09.022.

[47] D. Seifu, A. Kebede, F.W. Oliver, E. Hoffman, E. Hammond, C. Wynter, A. Aning, L. Takacs , L. Siu, J.C. Walker, G. Tessema, M.S. Seehra, “Evidence of ferrimagnetic ordering in FeMnO3 produced by mechanical alloying,” *Journal of Magnetism and Magnetic Materials*, vol. 212, no. 1–2, pp. 178–182, Mar. 2000, doi: 10.1016/S0304-8853(99)00787-8.

[48] S. Rayaprol and S. D. Kaushik, “Magnetic and magnetocaloric properties of FeMnO3,” *Ceramics International*, vol. 41, no. 8, pp. 9567–9571, Sep. 2015, doi: 10.1016/J.CERAMINT.2015.04.017.

[49] D. J. McClements, “Biopolymers in Food Emulsions,” *Modern Biopolymer Science*, pp. 129–166, Jan. 2009, doi: 10.1016/B978-0-12-374195-0.00004-5.

[50] B. Liu and X. Hu, “Hollow Micro- and Nanomaterials: Synthesis and Applications,” *Advanced Nanomaterials for Pollutant Sensing and Environmental Catalysis*, pp. 1–38, Jan. 2020, doi: 10.1016/B978-0-12-814796-2.00001-0.

[51] H. Chen, Y. Yu, H. L. Xin, K. A. Newton, M. E. Holtz, D. Wang, D. A. Muller, H. D. Abruña, and F. J. DiSalvo, “Coalescence in the Thermal Annealing of Nanoparticles: An in Situ STEM Study of the Growth Mechanisms of Ordered Pt−Fe Nanoparticles in a KCl Matrix,” *Chem. Mater*, vol. 25, 2013, doi: 10.1021/cm303489z.

[52] Y. P. Lin and N. L. Wu, “Characterization of MnFe2O4/LiMn2O4 aqueous asymmetric supercapacitor,” *Journal of Power Sources*, vol. 196, no. 2, pp. 851–854, Jan. 2011, doi: 10.1016/J.JPOWSOUR.2010.07.066.

[53] M. Toupin, T. Brousse, and D. Bélanger, “Influence of Microstucture on the Charge Storage Properties of Chemically Synthesized Manganese Dioxide”, Chem. Mater. 2002, 14, 9, 3946–3952

[54] J. H. Lim, D. J. Choi, H.-K. Kim, W. Il Cho, Y. S. Yoon, “Thin Film Supercapacitors Using a Sputtered RuO2 Electrode”, *J. Electrochem. Soc.* **2001**, *148*, A275.

[55] J. N. Broughton, M. J. Brett, “Electrochemical capacitance in manganese thin films with chevron microstructure”, *Electrochem. Solid-State Lett.* **2002**, *5*, DOI 10.1149/1.1516412.

[56] T. Dinh, F. Mesnilgrente, V. Conedera, N. A. Kyerematenq, D. Pech, “Realization of an Asymmetric Interdigitated Electrochemical Micro- Capacitor Based on Carbon Nanotubes and Manganese Oxide Realization of an Asymmetric Interdigitated Electrochemical Micro-Capacitor Based on Carbon Nanotubes and Manganese Oxide”, *J. Electrochem. Soc.* **2015**, *162*, A2016.

[57] M. Hallot, P. Roussel, and C. Lethien, “Sputtered LiNi0.5Mn1.5O4 Thin Films for Lithium-Ion Microbatteries,” *ACS Applied Energy Materials*, vol. 4, no. 4, pp. 3101–3109, Apr. 2021, doi: 10.1021/ACSAEM.0C02831/SUPPL_FILE/AE0C02831_SI_001.PDF.

[58] M. HALLOT, B. CAJA-NUNOZ, C. LEVIEL, O. LEBEDEV, R. RETOUX, J. AVILA, P. ROUSSEL, M. ASENCIO, C. LETHIEN, “Atomic Layer Deposition of a Nanometer-Thick Li3PO4Protective Layer on LiNi0.5Mn1.5O4Films: Dream or Reality for Long-Term Cycling?,” *ACS Applied Materials and Interfaces*, vol. 13, no. 13, pp. 15761–15773, Apr. 2021, doi: 10.1021/ACSAMI.0C21961/SUPPL_FILE/AM0C21961_SI_001.PDF.

[59] M. Hallot, A. Demortière, P. Roussel, and C. Lethien, “Sputtered LiMn1.5Ni0.5O4 thin films for Li-ion micro-batteries with high energy and rate capabilities,” *Energy Storage Materials*, vol. 15, pp. 396–406, Nov. 2018, doi: 10.1016/J.ENSM.2018.08.012.

[60] C. Arico, S. Ouendi, P. L. Taberna, P. Roussel, P. Simon, and C. Lethien, “Fast Electrochemical Storage Process in Sputtered Nb2O5 Porous Thin Films,” *ACS Nano*, vol. 13, no. 5, pp. 5826–5832, May 2019, doi: 10.1021/ACSNANO.9B01457/ASSET/IMAGES/LARGE/NN-2019-014578_0006.JPEG.

[61] S. Ouendi, K. Robert, D. Stievenard, T. Brousse, P. Roussel, and C. Lethien, “Sputtered tungsten nitride films as pseudocapacitive electrode for on chip micro-supercapacitors,” *Energy Storage Materials*, vol. 20, pp. 243–252, Jul. 2019, doi: 10.1016/J.ENSM.2019.04.006.

[62] J. A. Thornton, “Structure-Zone Models Of Thin Films,” *Modeling of Optical Thin Films*, vol. 0821, p. 95, Feb. 1988, doi: 10.1117/12.941846.

[63] J. A. Thornton, “Influence of apparatus geometry and deposition conditions on the structure and topography of thick sputtered coatings,” *Journal of Vacuum Science and Technology*, vol. 11, no. 4, p. 666, Dec. 2000, doi: 10.1116/1.1312732.

[64] A. M. Jacintha, A. Manikandan, K. Chinnaraj, S. A. Antony, and P. Neeraja, “Comparative Studies of Spinel MnFe2O4 Nanostructures: Structural, Morphological,

Optical, Magnetic and Catalytic Properties," *J Nanosci Nanotechnol*, vol. 15, no. 12, pp. 9732–9740, Dec. 2015, doi: 10.1166/JNN.2015.10343.

[65] H. L. Andersen, M. Saura-Múzquiz, C. Granados-Miralles, E. Canévet, N. Lock, and M. Christensen, "Crystalline and magnetic structure–property relationship in spinel ferrite nanoparticles," *Nanoscale*, vol. 10, no. 31, pp. 14902–14914, Aug. 2018, doi: 10.1039/C8NR01534A.

[66] A. A. Spivakov, C. R. Lin, E. S. Lin, Y. Z. Chen, and Y. T. Tseng, "Preparation and Magnetic Properties of Cobalt-Doped FeMn2O4 Spinel Nanoparticles," *Nanoscale Research Letters*, vol. 16, no. 1, p. 162, 2021, doi: 10.1186/S11671-021-03619-7.

LIST OF FIGURES AND FIGURE CAPTIONS

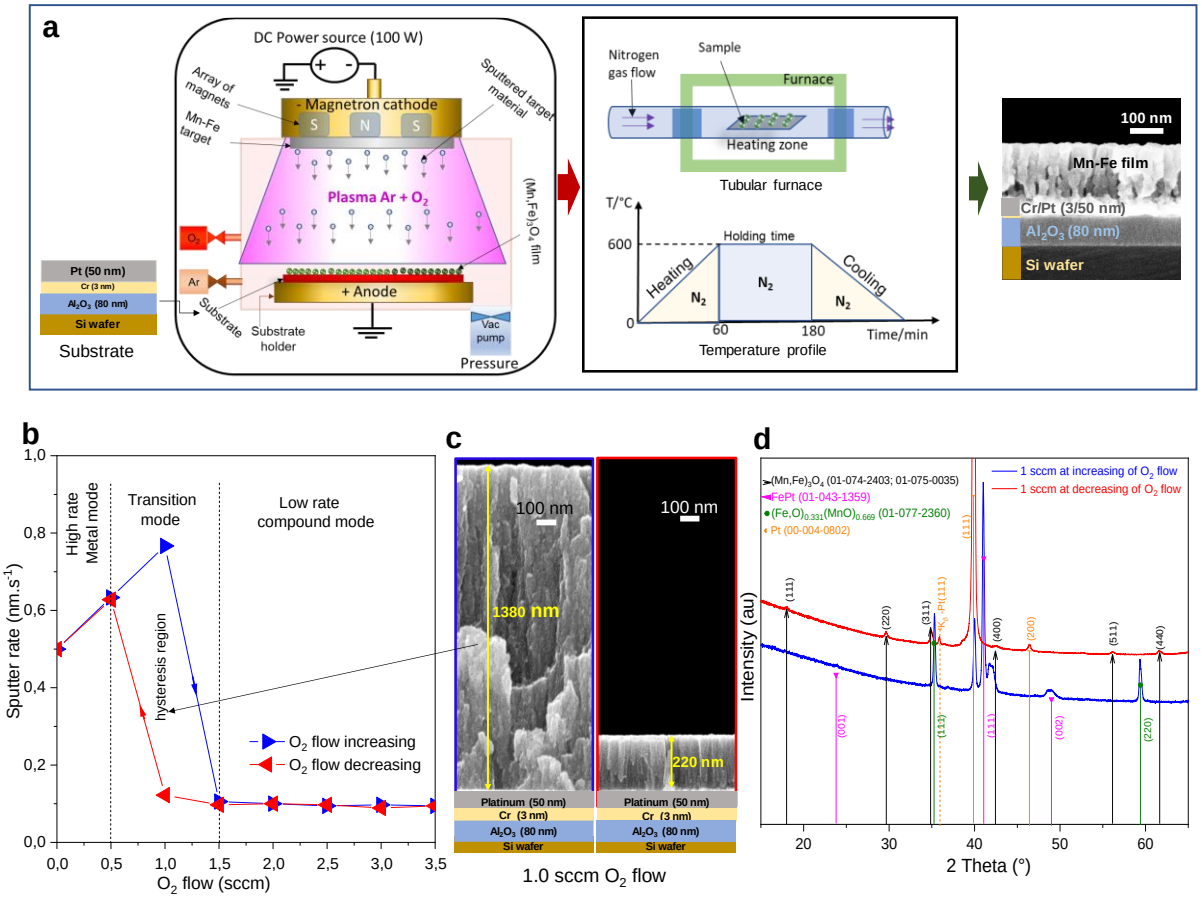

Fig. 1 | Overview of the spinel Mn-Fe film synthesis by two-step procedure: sputtering deposition and post-deposition ex-situ annealing. a. Schematic of the reactive magnetron DC sputtering process of the amorphous Mn-Fe deposited on a platinum-based current collector followed by the post-deposition *ex-situ* annealing and obtained Mn-Fe film. **b.** Deposition rate of the sputtered films at different reactive oxygen gas contents (blue line for sputtering at increasing O_2 flow, while red line for sputtering at decreasing O_2 flow) diluted in 50 sccm of argon flow with several other parameters fixed (operating power, pressure and deposition time of 100 W, 3 x 10^{-2} mbar, and 30 min respectively). **c**. SEM cross-section images of the as-sputtered film

at 1 sccm of O_2 flow diluted in 50 sccm of Ar (when increasing and decreasing of O_2 flow). **d**. Diffractogramms of the annealed Mn-Fe films in **1c**.

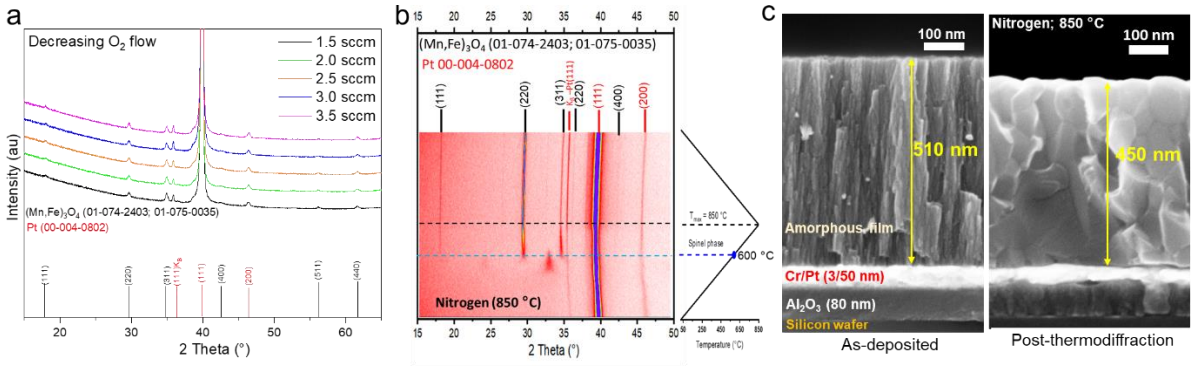

Fig. 2 | Phase evolution of the sputtered Mn-Fefilm. a. Diffractogramms of the annealed thin films deposited on a Pt current collector substrate sputtered at different O_2 flows diluted in 50 sccm of Ar and at room temperature with fixed operating power, pressure and deposition time of 100 W, 3 x 10^{-2} mbar, and 30 min respectively. **b.** 2D view (stacking of 1D) X-ray thermodiffractograms for the sputtered Mn-Fe (sample with 2 sccm of O_2 flow) heated from 50 °C to 850 °C under inert nitrogen gas environment during the *in situ* HT-XRD analysis **c.** SEM cross section images before and after the thermodiffraction analysis of the film.

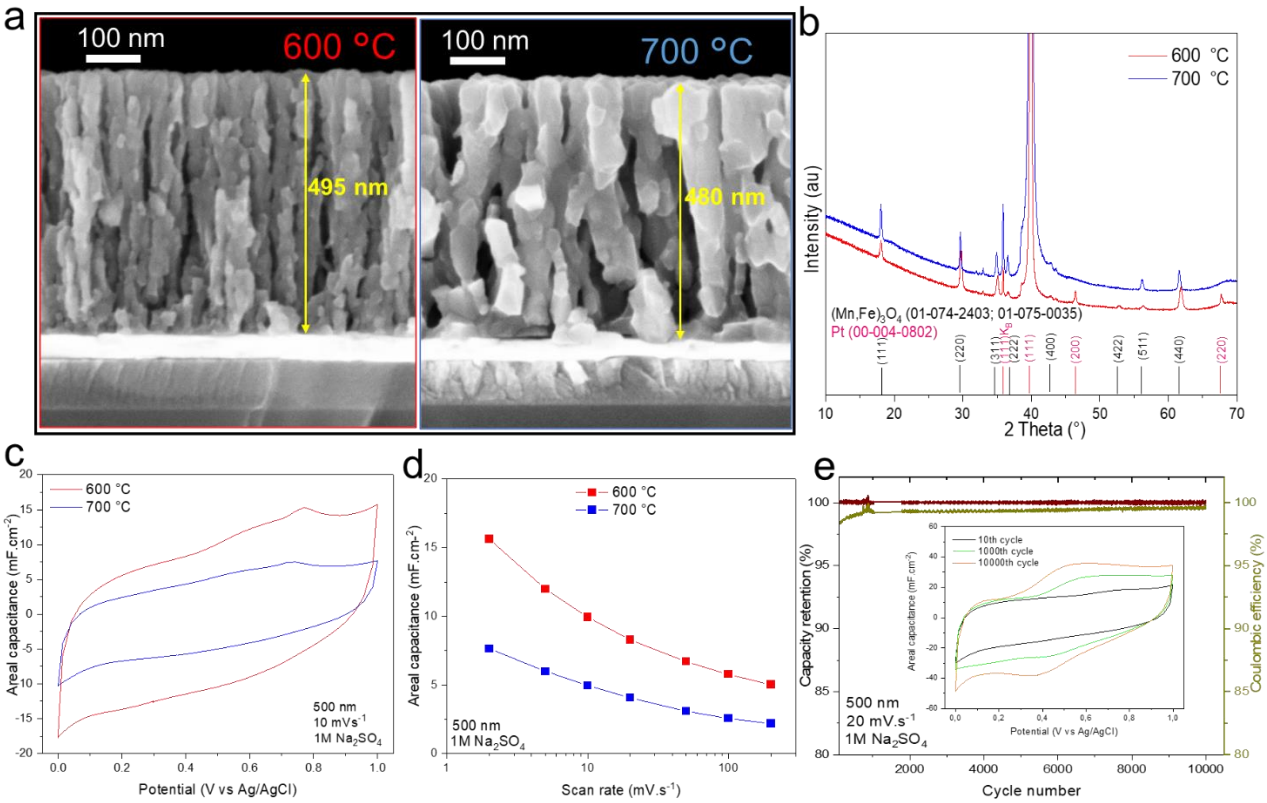

Fig. 3 | Optimization of post-deposition annealing temperature. a. SEM cross section images of Mn-Fe films (500 nm thick) annealed at 600 °C and 700 °C. **b**. XRD diffractograms of the films. **c**. CV plots of the films at 10 mV.s-^{1}. **d**. Evolution of the areal capacitance at different scan rates as the function of temperature. **e.** Capacity retention and coulombic efficiency as a function of the cycle number (inset, CVs of the 10th and 10 000th cycles).

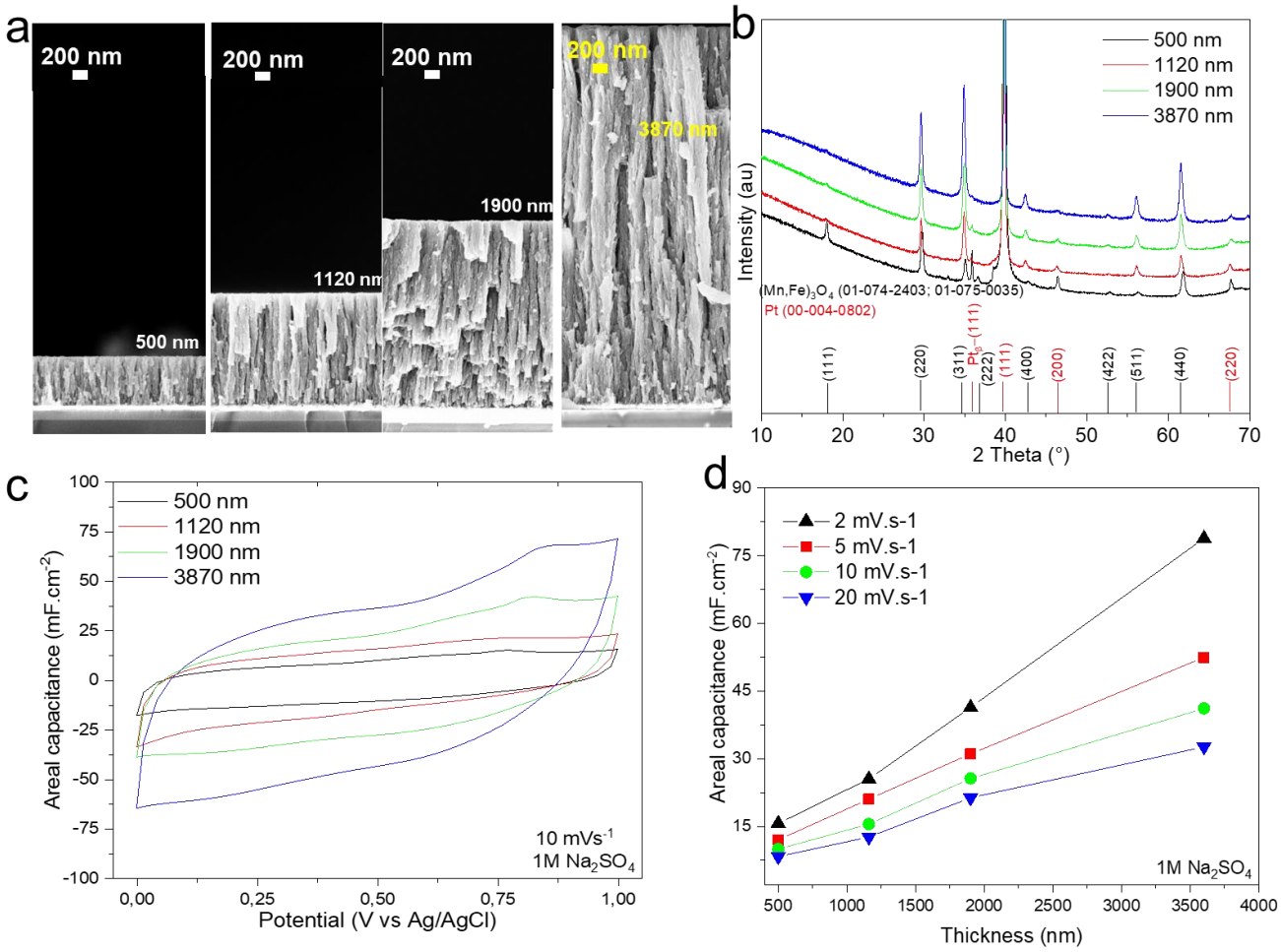

Fig. 4 | Electrochemical properties of the Mn-Fe spinel films in 1M Na_2SO_4 for various film thicknesses. a. SEM cross section analysis of the annealed films (from 500 nm to 3800 nm film thickness). **b**. XRD diffractograms of the various film thicknesses. **c**. CV plots of the films at 10 mV.s-1. d. Summary of the areal capacitance values for the various thicknesses at different scan rates, and **e**. Evolution of the areal capacitance as the function of the thickness.

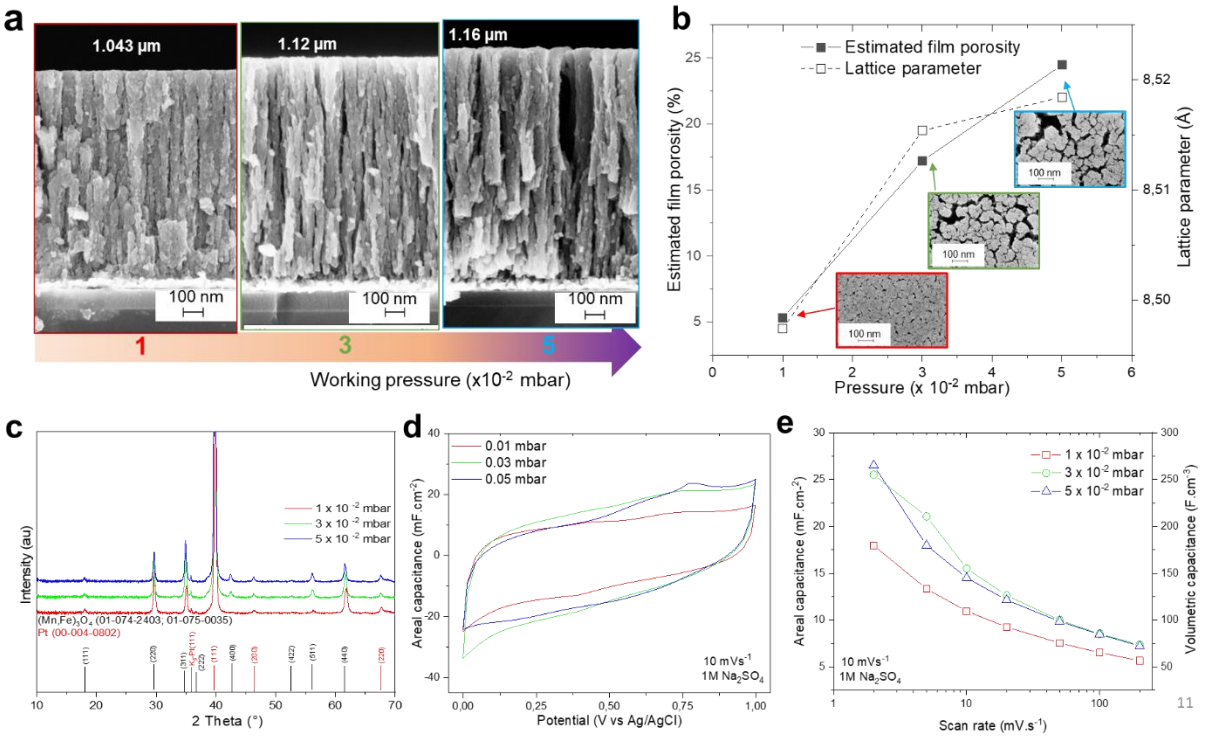

Fig. 5 | Structural, morphological and electrochemical analyses of 1 µm thick Mn-Fe spinel thin films sputtered at room temperature and different operating pressure from 1 x 10^{-2} to 5 x 10^{-2} with fixed operating power, O_2 and Ar flows of 100 W, 2 sccm and 50 sccm respectively and annealed at 600 °C during 2 h under nitrogen atmosphere. a. SEM cross section analysis of the annealed Mn-Fe films as a function of operating pressure. **c**. Evolution of the porosity and lattice parameter as function of the deposition pressure. c. XRD diffractograms of the films annealed films. **d**. CV plots of the films at 20 mV.s-^{1}. **e.** Summary of the areal and volumetric capacitance of various operating pressure at different scan rates.